



A NUMERICAL STUDY OF UNDER-DEPOSIT PITTING CORROSION IN SOUR PETROLEUM PIPELINES

Zhenjin Zhu, Keith W. Sand, Patrick J. Teevens
Broadsword Corrosion Engineering Ltd.

Copyright 2010 NACE International

Requests for permission to publish this manuscript in any form, in part or in whole must be in writing to NACE International, Publications Division, 1440 South Creek Drive, Houston, Texas 77084-4906.

The material presented and the views expressed in this paper are solely those of the author(s) and not necessarily endorsed by the Association. Printed in Canada

A NUMERICAL STUDY OF UNDER-DEPOSIT PITTING CORROSION IN SOUR PETROLEUM PIPELINES

Zhenjin Zhu, Keith W. Sand, Patrick J. Teevens

Broadsword Corrosion Engineering Ltd.
90 Commercial Drive, Calgary, Alberta, Canada T3Z 2A7

ABSTRACT

When the fluid velocity in petroleum pipelines is insufficient, solids including sand, corrosion products and non corrosion products will be deposited on metal surface, triggering localized pitting corrosion. Owing to the inherent difficulty to detect and design against, the pitting process is extremely insidious. Industry lacks a reliable preventive method to tackle this issue, leading to significant safety concerns. Statistics showed that 54% of pipeline failures in Alberta were attributed to internal corrosion in 2002. A predominant pitting corrosion takes place under the sour environment. Since most of the pipelines west of Highway 2 are sour, more attention needs to be paid in Alberta. Although a vast amount of research has been conducted on understanding internal corrosion of pipelines in the past years, fundamental mechanisms of localized pitting corrosion still remain unclear. In this paper, in-house proprietary codes were written using the Finite Element Method to simulate mass transfer governed, internal pitting corrosion under solids deposition in sour petroleum pipelines. The computational domain includes a hemispherical pit and a thin stagnant solution film under surface deposits. The moving mesh method was applied to track the pitting growth. To determine aqueous path migration of ions, the electrical field was calculated from the Poisson equation with electroneutrality. The concentration distribution of each chemical species in the shielded solution was obtained by solving transient diffusion equations. Based on the Nernst-Planck equation, pitting corrosion rates were consequently estimated. As well, the effects of operation parameters on pitting corrosion rates and incubation time were predicted, which can assist the industry to develop a proper pigging schedule and prevent pitting corrosion effectively. The anticipated scientific research with the objectives of establishing such a model is definitely original and innovative. As a result, advancements in ICPM which require a capability to assess corrosion under solids deposition will be a reality rather than the exception. This paper represents a major advancement in the science and engineering development needed for credible ICDA protocols to better predict petroleum pipeline internal corrosion behaviour.

Keywords: Finite Element Analysis, Moving mesh, Under-deposit pitting corrosion, Solids deposition, Sour petroleum pipeline, Nernst-Planck equation

BACKGROUND

Localized pitting corrosion primarily appears at metal surface with defects due to a breakdown of a passive film, micro-structural phase heterogeneity, mechanical discontinuity, as well as diffusion of chloride through porous oxide film. Pitting corrosion is extremely insidious. A pit can be triggered suddenly and does not show any correlation with the surrounding physical environment. Once pitting takes place, severe corrosion is concentrated on a very small area while the rest of the contact area is clean and corrosion-free. Such a great ratio of cathodic to anodic area enhances the corrosion rate further, making pitting corrosion self-propagating and catastrophic. Clearly safety of pipelines today has never been more heavily scrutinized. Hence, it is incumbent upon the pipeline operators to avoid these localized failures as they are simply a major disruption to many parties and stakeholders.

To date, a vast amount of research has been reported on understanding the fundamental mechanisms of localized corrosion as well as predicting general corrosion rates in sweet petroleum pipelines [1-4]. As early as 1937, Hoar [5] proposed a mechanistic model of “autocatalytic” pit propagation by considering the drop of pH inside the pit. More recently, de Waard et al. [6] developed internal corrosion models to estimate pitting corrosion rates as a function of system pressure, temperature, CO₂ partial pressure, and steel microstructure. Crolet et al. [7] investigated the probability of CO₂ pitting corrosion in oil wells through field tests. Nesic et al. [8-9] researched carbon dioxide corrosion of mild steel in the presence of protective iron carbonate films. Tan [10] utilized the wire beam electrode in conjunction with electrochemical noise resistance measurements to map the corrosion kinetics. Papavinasam [11-12] formulated internal pitting corrosion rates for oil and gas pipelines based on field test data. Nagatani [13] numerically simulated pit formation by assigning a zero-gradient of ions concentration at the boundaries on the metal surface excluding the pit.

Currently, more and more sour reservoirs are being developed by reason of limited petroleum resources in the world. Compared to a sweet environment with just CO₂, the presence of H₂S alters the corrosivity of the produced fluid in a sour system. Shannon and Boggs [14] revealed that the initial rate of corrosion of steel coupons by oil-water-H₂S mixtures depends on the H₂S concentration. Sardisco and Pitts [15] claimed that overall reaction was controlled partially by interface reaction and by transportation of ions/electrons across film during corrosion of iron under H₂S-CO₂-H₂O environment. Anderko and Young [16] proposed a comprehensive thermodynamic/kinetic computational model for H₂S-CO₂-Brine corrosion of carbon steel. Sun and Nesic [17] present a mechanism of H₂S corrosion of mild steel through glass cell experiments.

Scale formation has been recognized to be an important factor on preventing metal loss under sour environment. A variety of corrosion products have been hitherto observed in the scale, including amorphous ferrous sulfide FeS, Machinawite Fe_{1+x}S, cubic ferrous sulfide FeS, troilite FeS, pyrrhotite Fe_{1-x}S or FeS_{1+x}, smythite Fe_{3+x}S₃, as well as pyrite FeS₂ depending on the chemistry, structure, and formation of iron sulfide. Criaud and Fouillac [18] stated that the scale formed in the wells was FeS corrosion product due to reaction of dissolved sulfides with steel rather than a FeS mineral deposit from the produced brine. Martin and Annand [19] found that the presence of suspended FeS increases the corrosion rate because of an increase in the cathodic reaction through hydrogen adsorption by the suspended FeS particles. Lichti [20] concluded that sulfide films reduced corrosion rates even when present in minute amounts.

Although an abundance of research results has been published, the mechanism of localized pitting corrosion in sour environment is not well understood yet. Some conclusions are confusing and contradict one another. Since many failures have happened under the deposited solids in oil and gas

pipelines and petroleum industry has a desire to grasp a better understanding of localized pitting corrosion in sour environment, the authors of this paper were motivated to numerically simulate under-deposit pitting corrosion in sour petroleum pipelines.

THEORETICAL MODELING

Precisely predicting localized pitting corrosion rates in a sour environment is extremely challenging. This is because a variety of engineering and science disciplines have been involved, such as multiphase flow, multiphase mass transfer, chemical reactions, electrochemical reactions, thermodynamics, and iron sulfide chemistry. As well, these governing equations are time-dependent, nonlinear, and inter-related. Some of them are beyond the current modeling knowledge from first principle. As a first study, essential simplification assumptions were made through targeting those important chemical/physical phenomena only. Specifically, this work considered the pipelines to be made up of low-alloy carbon steel. Inside the shielded solution under the deposits, major chemical reactions were CO₂ hydration, carbonic acid dissociation, bicarbonate anion dissociation, H₂S dissolution, H₂S dissociation, and hydrogen sulfide anion dissociation. The chemical species mainly included CO₂, H₂CO₃, H⁺, HCO₃⁻, CO₃²⁻, H₂S, HS⁻, S²⁻, and Fe²⁺. Among them, H⁺, H₂CO₃, and Fe²⁺ were electroactive species, where H⁺ and H₂CO₃ were reduced at the cathodic surface but ferrous ion was the product of iron dissolution at anodic surface. No inhibitors were applied in the H₂S-CO₂-H₂O system. The gradient of electric potential in the solution was calculated in consideration of electroneutrality. As compared to mackinawite, pyrrhotite and symthite, the stoichiometric type FeS (e.g., cubic ferrous sulfide, troilite, greigite and pyrite) dominated the scale formation.

Pitting Corrosion Rate

Corrosion is the deterioration of a material through an electrochemical process [2-4]. Based on this concept, this paper defined the corrosion rate as the mass flux of Fe²⁺ ion leaving the metal surface. In a dilute solution, transportation of Fe²⁺ ion could be in the form of diffusion, electro-migration, as well as convection. As a consequence of negligible convection under the deposits, the Fe²⁺ flux was solved from the following Nernst-Planck equation:

$$\mathbf{J}_{Fe^{2+}} = -D_{Fe^{2+}} \nabla C_{Fe^{2+}} - \frac{Fz_{Fe^{2+}}}{\mathfrak{R}T} D_{Fe^{2+}} C_{Fe^{2+}} \nabla \phi \quad (1)$$

where \mathbf{J} denotes the mass flux in mol/(m²·s); D the diffusivity in m²/s; C the concentration in mol/L; F the Faraday's constant in C/mol_e; z the valence in mol_e/mol; \mathfrak{R} the ideal gas constant in J/(mol·K); T the absolute temperature in K; and Φ symbolizes the electric potential in V. Once the distributions of Fe²⁺ ion and electrical field in the solution were computed, pitting corrosion rate could be acquired.

Fe²⁺ Ion Transportation

Conservation of Fe²⁺ ion in the solution was governed by Fick's Second Law which takes the general form as follows:

$$\frac{\partial C}{\partial t} = -\nabla(\mathbf{J}) + R \quad (2)$$

where R represents the source term of chemical reactions in the solution. In this context, generation of Fe^{2+} ion through electrochemical reactions at metal surface was not applied as the source term. Instead, it was taken into account via the boundary conditions. In other words, the boundary condition of Fe^{2+} ion at anode was assigned from the anodic corrosion current density, whereas a zero concentration of Fe^{2+} ion was applied at cathode as a consequence of scale formation. Initially, the concentration of Fe^{2+} ion in the shielded solution was assumed to be identical to that of the bulk solution in chemical equilibrium.

Electrochemical Reactions

Via a multi-step mechanism, the electrochemical reaction in the anode is expressed as:



Once the electrical potential at the anode is acquired, the anodic corrosion current density can be calculated by the Tafel's law. That is,

$$i_{Fe^{2+}} = i_{0,Fe^{2+}} \cdot 10^{\frac{\phi_a - \phi_{rev,Fe^{2+}}}{b_{Fe^{2+}}}} \quad (4)$$

where $i_{Fe^{2+}}$ represents current density of iron oxidation in A/m^2 ; $i_{0,Fe^{2+}}$ signifies the exchange current density of iron oxidation in A/m^2 ; Φ_a denotes anodic potential in V; Φ_{rev} symbolizes a reversible potential of iron oxidation in V; and b is the Tafel slope of oxidation in V. In turn, the exchange current density of iron oxidation is given by [8]

$$i_0 = i_{0,ref} \left(\frac{C_{H^+}}{C_{H^+,ref}} \right)^{a_1} \cdot \left(\frac{C_{CO_2}}{C_{CO_2,ref}} \right)^{a_2} \cdot e^{\frac{-\Delta H}{R} \left(\frac{1}{T} - \frac{1}{T_{ref}} \right)} \quad (5)$$

where $i_{0,ref}$ symbolizes the reference exchange current density; $C_{H^+,ref}$ and $C_{CO_2,ref}$ are the reference hydrogen ion and carbon dioxide concentration, respectively. Hence, the surface concentrations of H^+ and CO_2 contribute to corrosion rate through the exchange current density. When the anodic corrosion current density is achieved, the mass flux of the iron ion at anode will be determined through

$$J_{Fe^{2+}} = \frac{i_{Fe^{2+}}}{n_{Fe^{2+}} F} \quad (6)$$

At the cathode, oxygen's influence on the corrosion process is through the oxygen reduction reaction. Nonetheless, transport of oxygen is very rare unless there is an operational upset and incomplete de-oxygenation of water mixed into the oil and gas pipeline systems. As a result, oxygen reduction is negligible under a very small oxygen concentration. Additionally, this study neglected reduction of water which is important only in high overpotential regions such as when the pH is greater than 5 and partial pressure of CO_2 is far less than 1 bar as per similar work performed by Nestic et al. [21]. That is, the H^+ reduction and H_2CO_3 reduction are the two cathodic reactions.



The partial cathodic corrosion current densities of H^+ reduction and H_2CO_3 reduction were determined from a general form [8] as follows:

$$i_c = i_0 \cdot 10^{\frac{\phi_c - \phi_{rev}}{b}} \cdot \eta_{Scale} \quad (9)$$

where i_c stands for the current density of any cathodic reaction in A/m^2 ; i_0 the exchange current density of cathodic reaction in A/m^2 ; Φ_c cathodic potential in V; Φ_{rev} a reversible potential of cathodic reaction in V; b the Tafel slope of cathodic reaction in V; and η_{scale} a scale factor at cathode. The exchange current densities of H^+ and H_2CO_3 reduction at cathode were obtained from Eq. (5) as well.

Scale Factor

The scale behaves as a barrier for ions infusion/effusion from/to the external solution-scale side to/from the internal scale-metal side. Here, the scale factor was approximated using the volumetric porosity of the scale which was given by [8]

$$\eta_{Scale} = \frac{V_{void}}{V_{total}} = 1 - \frac{V_{FeCO_3(s)} + V_{FeS(s)}}{V_{total}} = 1 - \frac{C_{FeCO_3(s)} \cdot M_{FeCO_3(s)}}{\rho_{FeCO_3(s)}} - \frac{C_{FeS(s)} \cdot M_{FeS(s)}}{\rho_{FeS(s)}} \quad (10)$$

where M and ρ represent the molecular mass and the density, respectively. Determination of the concentrations of the precipitated $FeCO_3$ and FeS were below described. First, the solubility product constants (K_{sp}) of $FeCO_3$ and FeS were collected. Following this, the molar concentrations of Fe^{2+} , S^{2-} , and CO_3^{2-} close to the cathode were calculated. Subsequently, the precipitated amount of $FeCO_3$ and FeS was solved from [22-24]

$$(C_{Fe^{2+}} - C_{FeCO_3(s)}) \times (C_{CO_3^{2-}} - C_{FeCO_3(s)}) = K_{sp,FeCO_3} \quad (11)$$

$$(C_{Fe^{2+}} - C_{FeS(s)}) \times (C_{S^{2-}} - C_{FeS(s)}) = K_{sp,FeS} \quad (12)$$

Consequently, the volumetric porosity of the scale was obtained. Furthermore, the criterion to determine whether $FeCO_3$ and FeS will be spontaneously precipitated during scale growth was a negative Gibbs free energy change. Namely,

$$\Delta G = \Delta G^0 + RT \ln Q_c < 0 \quad (13)$$

where ΔG^0 , R , T and Q_c represent standard free-energy change, gas constant, absolute temperature, and reaction quotient, respectively.

Concentration of H^+ Ion and Other Chemical Species

Distribution of contribution of the H^+ ion in the shielded solution was computed from Eq. (2) as well. When the gaseous carbon dioxide was dissolved in the solution, its concentration was calculated using

the solubility and partial pressure of carbon dioxide in the system. Through the aqueous carbon dioxide hydration, carbonic acid was generated. That is,



where k_f and k_b symbolize the rate constants of forward and backward reactions, respectively. Subsequently, carbonic acid partially dissociated to form bicarbonate and carbonate ions through the following two steps:



The aqueous H_2S is an additional reservoir of H^+ ions as a weak acid. The initial concentration of H_2S in the solution was determined from its solubility constant and partial pressure in the system. The aqueous H_2S partly dissociates in two steps:



As a result, the generation rate of H^+ ion concentration was expressed as

$$\begin{aligned} R_{H^+} = & K_{f,ca} \cdot C_{H_2CO_3} - K_{b,ca} \cdot C_{H^+} \cdot C_{HCO_3^-} + K_{f,bi} \cdot C_{HCO_3^-} - K_{b,bi} \cdot C_{H^+} \cdot C_{CO_3^{2-}} \\ & + K_{f,HS} \cdot C_{H_2S} - K_{b,HS} \cdot C_{H^+} \cdot C_{HS^-} + K_{f,bs} \cdot C_{HS^-} - K_{b,bs} \cdot C_{H^+} \cdot C_{S^{2-}} \end{aligned} \quad (19)$$

Similarly, distribution of concentration of other chemical species could be determined as well.

Gradient of Electrochemical Potential

Electric field in the solution was governed by the following Poisson's equation:

$$\nabla^2 \phi = -\frac{F}{\varepsilon} \sum_{i=1}^n z_i c_i \quad (20)$$

where ε represents the dielectric constant. In terms of electro-neutrality, a perfect balance between the positively and negatively charged species was expected everywhere in the solution, leading to

$$\sum_{i=1}^n z_i c_i = 0 \quad (21)$$

Hence, distribution of electrochemical potential gradient was computed from

$$\nabla^2 \phi = 0 \quad (22)$$

For low-alloy carbon-steel pipelines, the anodic potential was achieved from the Pourbaix diagram [25]. Specifically,

$$\phi_a = -0.440 + 0.0295 \times \log_{10}(C_{Fe^{2+}}) \quad (23)$$

The cathodic potential was solved from the balance between the anodic current and the sum of all cathodic currents. Namely,

$$i_{a,Fe^{2+}} = i_{c,H^+} + i_{c,HCO_3^-} \quad (24)$$

OVERALL SIMULATION PROCEDURE

General Procedure

As aforementioned, pitting corrosion was governed by a set of time-dependent, non-linear equations coupled with concentration of each chemical species, source term of each chemical reaction, corrosion current densities at the anode and cathode, and gradient of electrical potential. An iteration method with an implicit scheme had to be applied for this study. Prior to time evolution, all material properties and physical constants were collected. During iteration, the computational domain was firstly updated based on the corrosion rate acquired from a previous iteration. After electric potentials at the anode and cathode were determined, gradients of electrical potential in the solution were achieved by solving the Poisson's equation with electroneutrality. Subsequently distribution of concentration of each species was obtained by applying chemical reaction rate as the source term whereas electrochemical reaction rates were assigned as the boundary conditions. As a result, the growth rate of a pit was calculated. Time evolution would not cease until the pit size approached the size of the deposited particle.

Finite Element Method and Moving Mesh

In this paper, the pit was simplified to be hemispherical. As demonstrated in Figure 1, the computational domain consisted of the pit as well as a thin solution film under a settled particle with a flat bottom. The Galerkin Finite Element Method was employed [26-28] to derive the variational formula of the partial differential equations as well as corresponding boundary values. The mesh was generated using the linear triangular elements in the Axisymmetric coordinate system. The moving mesh method [29-30] with a fixed node number was applied to track the pit growth.

Initial and Boundary Conditions

Initially, concentration of each species in the shielded solution was assumed to be in chemical equilibrium and identical to that of bulk liquid. Based on the given partial pressure of CO₂ and H₂S in the system, the initial CO₂ and H₂S concentrations were first determined. From the equilibrium constants of each chemical reaction which were summarized in Table 1, the initial concentrations of H₂CO₃, HCO₃⁻, CO₃²⁻, H₂S, HS⁻, and S²⁻ were then obtained. To solve the distribution of concentration

of each chemical species, an impermeable condition was applied at the left and top boundaries. The concentration at the right boundary was considered to be equal to that of the bulk. At the anode and cathode, the Neumann boundary conditions were applied for those species without chemical reactions or electrochemical reactions. The corrosion current densities were utilized only for those electroactive species. A zero concentration was employed for the iron ion at the cathode. With respect to the electrical field, the Dirichlet boundary conditions were applied at anode and cathode whereas a zero-gradient potential was assigned at other boundaries.

RESEARCH CONTENTS AND RESULTS ANALYSIS

In this context, the CO₂-H₂S-H₂O system was designed with an initial pit radius of 48 μm and a solution film thickness of 30 μm. The base case has a uniform temperature of 25 °C, CO₂ partial pressure of 1 bar, and H₂S partial pressure of 0.75 bar.

Distribution of Electrochemical Potential

Figure 2 illustrates distribution of electrochemical potential inside the pit with anodic potential of -0.562 V and cathodic potential of -0.290 V. Figure 3 and Figure 4 demonstrate the gradients of electrical potential in the radial and vertical directions, respectively. It is interesting to note that there is a high potential gradient at the pit mouth.

Distribution of Ions Concentration

Figure 5 displays distribution of iron ions in the solution. As expected, a higher iron ion concentration is located at the anode, which effuses into the bulk solution through the pit mouth and then a micro-channel between the settled solids and the metal surface. Apparently, a deep pit or a long micro-channel will make iron ion effusion difficult, causing an elevated iron ion concentration inside the pit. Figure 6 depicts the distribution of hydrogen ion concentration. It is observed that a high H⁺ ion concentration is inside the pit, leading to a low pH value. Figures 7 and 8 plot the distribution of carbonate ions and S²⁻ ions, respectively. It can be seen that anions are infusing into the pit from the bulk solution.

Pitting Corrosion Rates

Figure 9 describes the pitting growth rate of the base case with an initial iron ion concentration of 0.05 mg/L. It is found that the corrosion rate is very small at the beginning. Approximately several months later, the corrosion rate increases remarkably. Figure 10 illustrates variation of the pH value at the anode over time, indicating that pH keeps decreasing inside the pit. Figure 11 reveals the variations of electrical potentials at anode and cathode. It is demonstrated that the anodic potential keeps increasing whereas cathodic potential decreases continuously. Figure 12 depicts the corrosion current densities at anode and cathode, respectively. It is revealed that during the incubation period, the corrosion current densities are much less.

When the pit size is close to the deposited particle size, the effect of convection on the ion transportation cannot be neglected anymore. The convection will be able to take the generated H⁺ ions away, which makes H⁺ ions difficult to be accumulated inside the pit. As a consequence, the “autocatalytic” pitting phenomenon may not take place. In other words, the pit may grow unstably or cease to grow depending on the degree of influence of convection on ions transportation. If the suspended or dissolved solids keep accumulating at this site, a corrosive environment (with a low pH value) under the deposited solids

can be maintained for pitting propagation further. Pipeline failures tend to be inevitable only when the solids lump is large enough as well as can stay the same site longer than the incubation time.

Effects of Environmental Conditions on Pitting Corrosion

Table 2 lists the cases designed to comprehend the effects of environmental parameters on sour pitting corrosion. Figure 13 illustrates the pitting corrosion rates with respect to the initial iron ion concentration. It is noted that a low initial iron ion concentration in both the pit pre-cursor and the bulk fluid results in a long incubation period for pitting. Figure 14 plots the pitting corrosion rates as a function of H₂S partial pressure when the CO₂ partial pressure was fixed at 1 bar. It is demonstrated that as the H₂S partial pressure increases, the pitting corrosion rate will be raised under a fixed CO₂ partial pressure. Figure 15 shows the effect of CO₂ partial pressure on pitting corrosion rates when H₂S partial pressure was fixed at 0.75 bar. As well, the pitting corrosion rates are boosted under an elevated partial pressure of CO₂. Figure 16 depicts the influence of system temperature on the pitting corrosion rates. When temperature increases from 25 °C to 75 °C, pitting corrosion will be enhanced accordingly.

CONCLUSIONS

This paper conducted a numerical study to predict pitting corrosion rates under solids deposition in a CO₂-H₂S-H₂O system. Results exhibit that an incubation period is necessary for pitting to take place. The incubation time will be extended under a low iron ion concentration, lower system temperature, as well as lower partial pressure of carbon dioxide and hydrogen sulfide. If the size of the deposited solids lump is large enough, an ideal under-deposit corrosive environment can be maintained for accelerated pitting propagation, leading to inevitable pipeline failures.

ACKNOWLEDGEMENTS

The authors are grateful to the Alberta Ingenuity Funds for their financial support of this research project.

REFERENCES

1. S. Netic, Key issues related to modeling of internal corrosion of oil and gas pipelines – A review, *Corros. Sci.*, 49 (2007) 4308-4338.
2. P. Marcus, *Corrosion mechanisms in theory and practice*, Second Edition, Marcel Dekker, Inc., New York, 2002.
3. H. H. Uhlig, *Corrosion handbook*, John Wiley & Sons, Inc., New York, 1948.
4. M. G. Fontana, *Corrosion engineering*, McGraw-Hill Inc., 1986.
5. T. P. Hoar, *Electrode process*, Butterworths, London, 1961.
6. C. de Waard, D. E. Milliams, Carbonic acid corrosion of steel, *Corrosion*, 31 (5) (1975) 177-181.
7. J. L. Crolet, N. Thevenot, and A. Dugstad, Role of free acetic acid on the CO₂ corrosion of steels, *NACE Corrosion 99*, Paper #24, Houston, Texas, 1999.
8. M. Nordsveen, S. Netic S, R. Nyborg, A. Stangeland, A mechanistic model for carbon dioxide corrosion of mild steel in the presence of protective iron carbonate films –Part 1: Theory and verification, *Corrosion*, 59 (5) (2003) 443-456.

9. S. Netic, K. L. J. Lee, A mechanistic model for carbon dioxide corrosion of mild steel in the presence of protective iron carbonate films—Part 3: film growth model, *Corrosion*, 59 (7) (2003) 616-628
10. Y. J. Tan, S. Bailey, B. Kinsella, A. Lowe, Mapping corrosion kinetics using the wire beam electrode in conjunction with electrochemical noise resistance measurements, *J. Electrochem. Soc.*, 147 (2) (2000) 530-539.
11. S. Papavinasam, R. W. Revie, and A. Doiron, Predicting internal pitting corrosion of oil and gas pipelines: Review of corrosion science models, NACE Corrosion 2005, Paper #5643, Houston, Texas, 2005.
12. S. Papavinasam, W. Friesen, R. W. Revie, and A. Doiron, Predicting internal pitting corrosion of oil and gas pipelines: Review of corrosion engineering approach, NACE Corrosion 2005, Paper #5645, Houston, Texas, 2005.
13. T. Nagatani, Scaling structure of pit profile in pitting corrosion, *J. Phys. Soc. Jpn.*, 60 (1991) 3997-4000.
14. D. W. Shannon, J. E. Boggs, Factors affecting the corrosion of steel by oil-brine-hydrogen sulfide mixtures, *Corrosion*, 15 (1959) 299-302.
15. J. B. Sardisco, R. E. Pitts, Corrosion of iron in an H₂S-CO₂-H₂O system mechanism of sulfide film formation and kinetics of corrosion reaction, *Corrosion*, 21(8) (1965) 245-253.
16. A. Anderko, R. D. Young, Simulation of CO₂/H₂S corrosion using thermodynamic and electrochemical models, *Corrosion/99*, Paper 31, 1999.
17. W. Sun, S. Netic, A mechanistic model of H₂S corrosion of mild steel, NACE Corrosion 2007, Paper #07655, 2007.
18. A. Criaud, C. Fouillac, Sulfide scaling in low-enthalpy geothermal environments: a survey, *Geothermics*, 18(1-2) (1989) 73-81.
19. R. L. Martin, R. R. Annand, Accelerated corrosion of steel by suspended iron sulfides in brine, *Corrosion*, 36 (1981) 297-301.
20. K. A. Lichti, S. Soylemezoglu, K. D. Cunliffe, Geothermal corrosion and corrosion products, *Proceeding of the New Zealand Geothermal Workshop 1981*, 103-108, 1981.
21. S. Nešić, H. Li, J. Huang, D. Sormaz, An open source mechanistic model for CO₂/H₂S Corrosion of carbon steel, NACE Corrosion 2009, Paper # 09572, Atlanta, Georgia, 2009.
22. J. C. Cowan, D. J. Weintritt, *Water-formed scale deposits*, Gulf Publishing Company, 1976.
23. L. E. Bagander, R. Carman, In situ determination of the apparent solubility product of amorphous iron sulfide, *Applied Geochemistry*, 9 (1994) 379-386.
24. P. Benezeth, J. L. Dandurand, J. C. Harrichoury, Solubility product of siderite (FeCO₃) as a function of temperature (25—250 °C), *Chemical Geology*, 265 (1-22) (2009) 3-12.
25. M. Pourbaix, *Atlas of electrochemical equilibria in aqueous solutions*, NACE Internal, Cebelcor, 1974.
26. T. J. Chung, *Computational fluid dynamics*, Cambridge University Press, 2002.
27. S. Gavrilov, M. Vankeerberghen, G. Nelissen, J. Deconinck, Finite element calculation of crack propagation in type 304 stainless steel in diluted sulphuric acid solution, *Corros. Sci.*, 49 (2007) 980-999.
28. Z. Zhu, J. Wang, D. F. James, C. B. Park, Finite element analysis of shear-thinning flow of polymer-gas solution in a hyperbolic convergent slit die, PPS-2007 Regional conference, Shanghai, China, July 12-14, 2007.
29. Z. Zhu, D. Xu, C. B. Park, R. G. Fenton, Finite element analysis of cell coarsening in plastic foaming, *J. Cell. Plast.*, 41 (2005) 475-486.
30. Z. Zhu, C. B. Park, J. Zong, Challenges to the formation of nano cells in foaming processes, *Int. Polym. Proc.*, 23 (3) (2008) 270-276.

31. J. E. Oddo, M. B. Tomson, Simplified calculation of CaCO₃ saturation at high temperatures and pressures in brine solutions, SPE of AIME, Richardson, TX, 1583-1590, 1982.
32. D. A. Palmer, R. van Eldik, The chemistry of metal carbonato and carbon dioxide complexes, Chem. Rev., 83(6) (1983) 651-731.
33. Comprehensive Chemical Kinetics, Vol. 6, Elsevier Publishing Co., Amsterdam, Netherlands, 283-284, 1972.
34. E. Hogfeldt, Stability constants of metal-ion complexes, Part A: Inorganic Ligands, IUPAC Chemical Data Series, No. 21, Pergamon Press, Oxford, 1982.
35. Y. K. Kharaka, E. H. Perkins, et al., Solmineq 88: A computer program for geochemical modeling of water rock interactions, Menlo Park, CA, Alberta Research Council, 1989.

TABLE 1: EQUILIBRIUM CONSTANTS FOR CHEMICAL REACTIONS

| Chemical Reaction | Formula | Description of Equilibrium Constant | Source of Equilibrium Constant |
|-------------------------------------|--|--|---------------------------------------|
| Dissolution of CO ₂ | $CO_{2(g)} \Leftrightarrow CO_{2(aq)}$ | $K_{sol} = C_{CO_2} / P_{CO_2}$ | [31] |
| CO ₂ hydration | $CO_{2(aq)} + H_2O \underset{k_{b,hy}}{\overset{k_{f,hy}}{\Leftrightarrow}} H_2CO_3$ | $K_{hy} = C_{H_2CO_3} / C_{CO_2}$ | [32] |
| Carbonic acid dissociation | $H_2CO_3 \underset{k_{b,ca}}{\overset{k_{f,ca}}{\Leftrightarrow}} H^+ + HCO_3^-$ | $K_{ca} = C_{H^+} C_{HCO_3^-} / C_{H_2CO_3}$ | [31, 33] |
| Bicarbonate anion dissociation | $HCO_3^- \underset{k_{b,bi}}{\overset{k_{f,bi}}{\Leftrightarrow}} H^+ + CO_3^{2-}$ | $K_{bi} = C_{H^+} C_{CO_3^{2-}} / C_{HCO_3^-}$ | [31, 8] |
| Dissolution of hydrogen sulfide | $H_2S_{(g)} \Leftrightarrow H_2S_{(aq)}$ | $K_{sol} = C_{H_2S} / P_{H_2S}$ | [34] |
| Hydrogen sulfide dissociation | $H_2S \underset{k_{b,HS}}{\overset{k_{f,HS}}{\Leftrightarrow}} H^+ + HS^-$ | $K_{hs} = C_{H^+} C_{HS^-} / C_{H_2S}$ | [35, 8] |
| Hydrogen sulfide anion dissociation | $HS^- \underset{k_{b,bs}}{\overset{k_{f,bs}}{\Leftrightarrow}} H^+ + S^{2-}$ | $K_{bs} = C_{H^+} C_{S^{2-}} / C_{HS^-}$ | [35, 8] |

TABLE 2: CASES OF ENVIRONMENTAL PARAMETERS ON PITTING CORROSION RATES

| Case | System Temperature | Partial Pressure of H₂S | Partial Pressure of CO₂ | Initial Iron Ion Concentration |
|-------------|---------------------------|---|---|---------------------------------------|
| 1 | 25 °C | 0.75 bar | 1.0 bar | 0.050 mg/L |
| 2 | 25 °C | 0.75 bar | 1.0 bar | 0.500 mg/L |
| 3 | 25 °C | 0.75 bar | 1.0 bar | 0.005 mg/L |
| 4 | 25 °C | 0.75 bar | 0.9 bar | 0.050 mg/L |
| 5 | 25 °C | 0.75 bar | 0.8 bar | 0.050 mg/L |
| 6 | 25 °C | 1.00 bar | 1.0 bar | 0.050 mg/L |
| 7 | 25 °C | 0.50 bar | 1.0 bar | 0.050 mg/L |
| 8 | 50 °C | 0.75 bar | 1.0 bar | 0.050 mg/L |
| 9 | 75 °C | 0.75 bar | 1.0 bar | 0.050 mg/L |

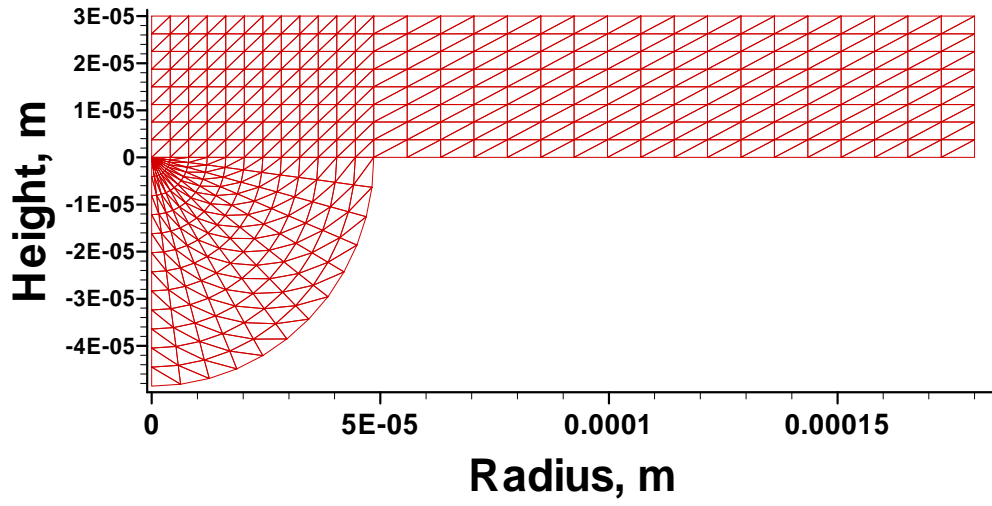


Figure 1 - Mesh generation of computational domain

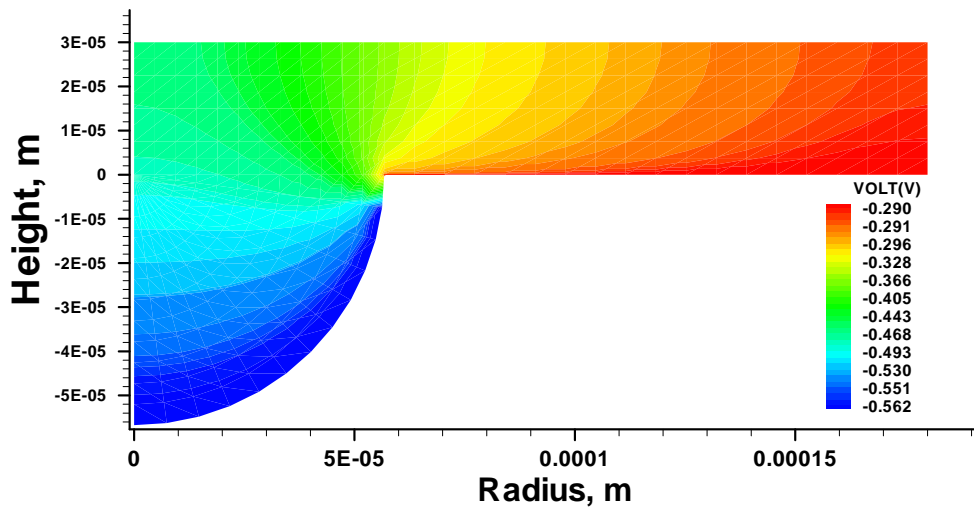


Figure 2 - Distribution of electrical potential in the shielded solution

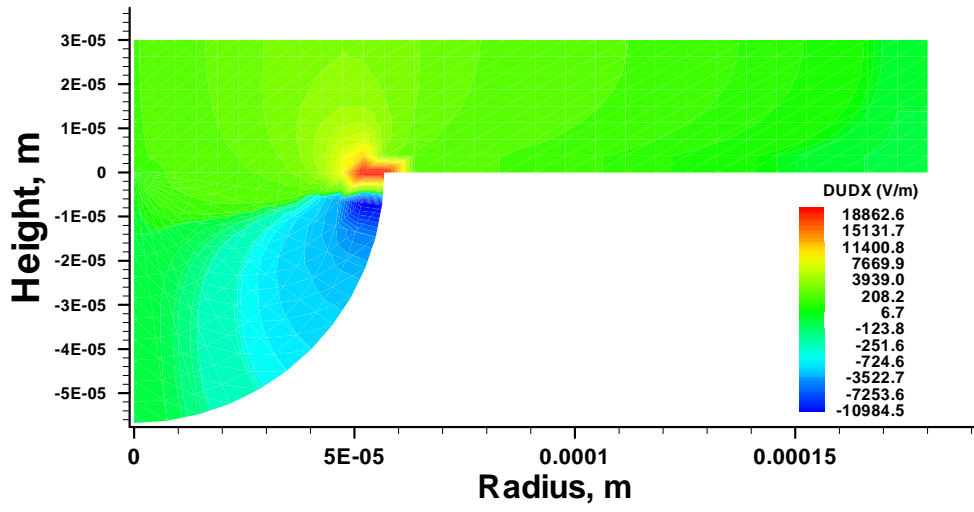


Figure 3 - Gradient of electrical potential in radial direction

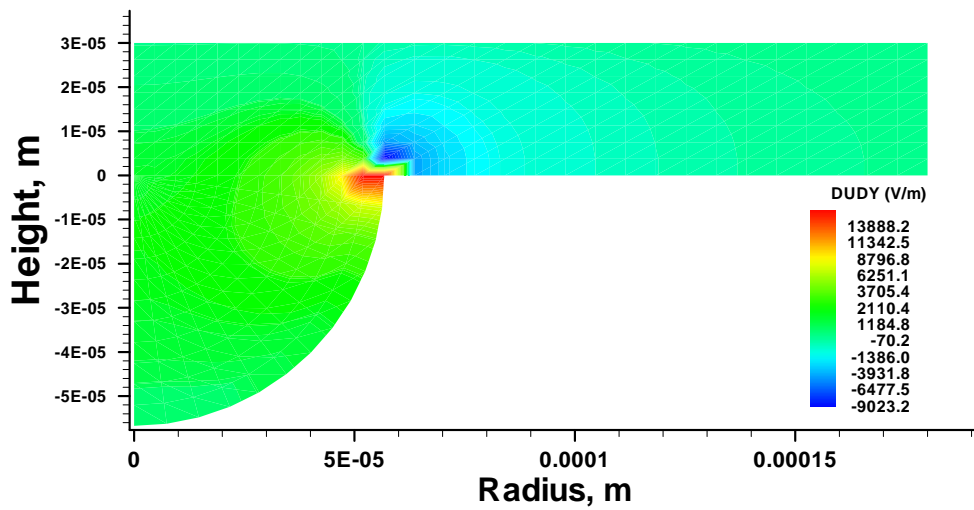


Figure 4 - Gradient of electrical potential in vertical direction

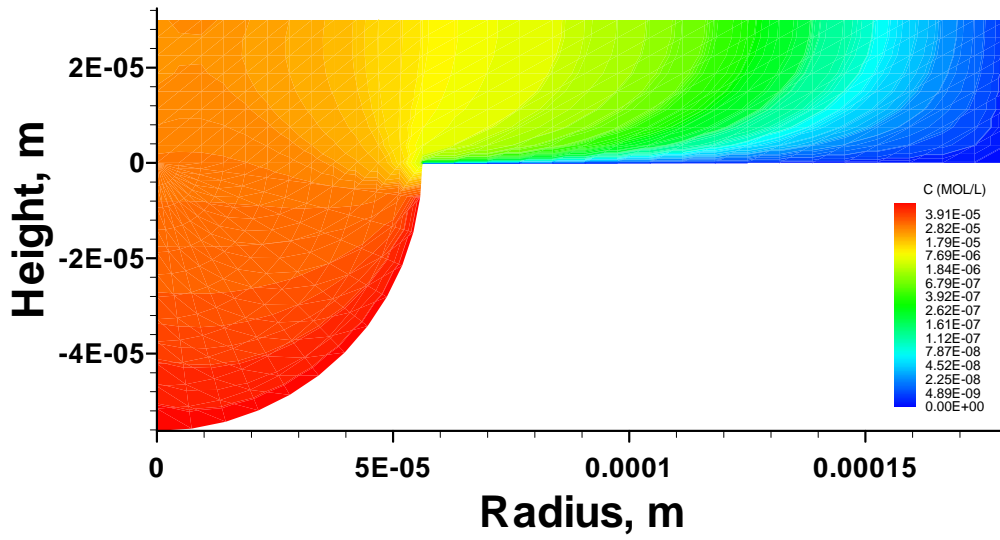


Figure 5 - Distribution of Fe^{2+} ion in the solution

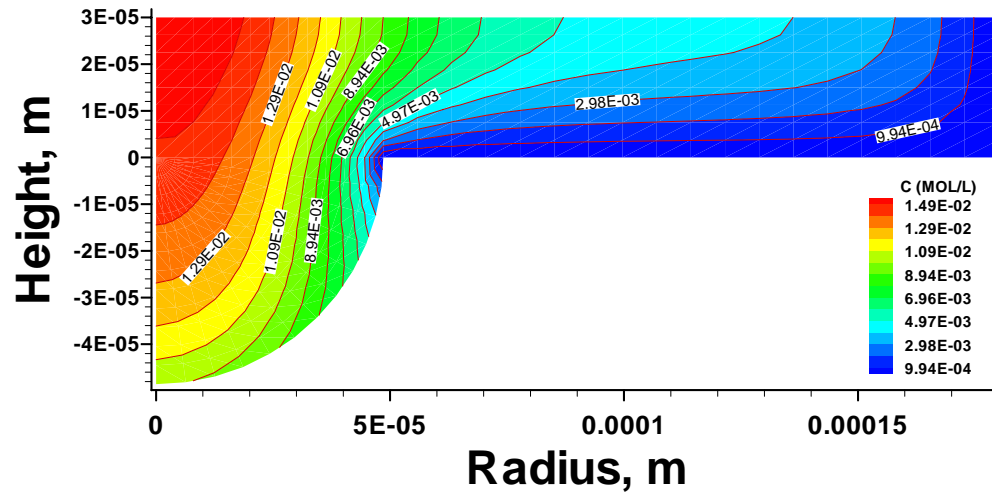


Figure 6 - Distribution of H^+ ion in the solution

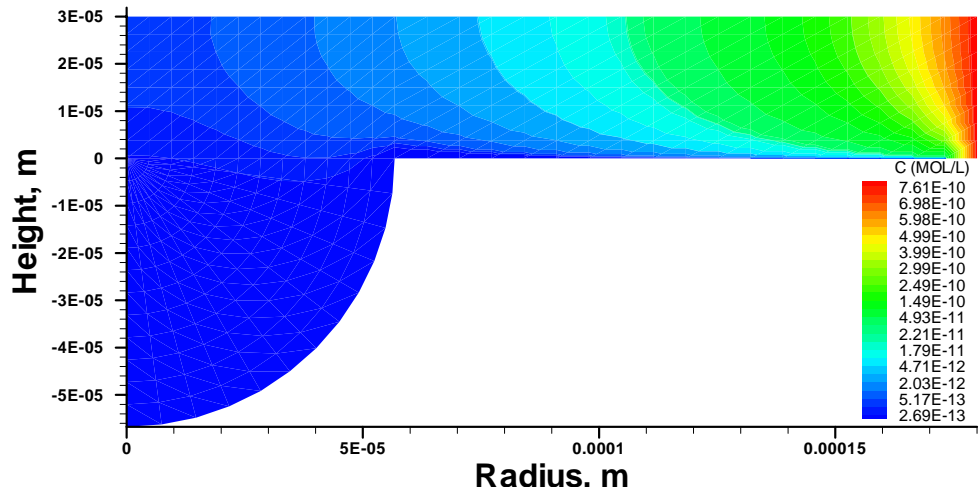


Figure 7 - Distribution of CO_3^{2-} ion in the solution

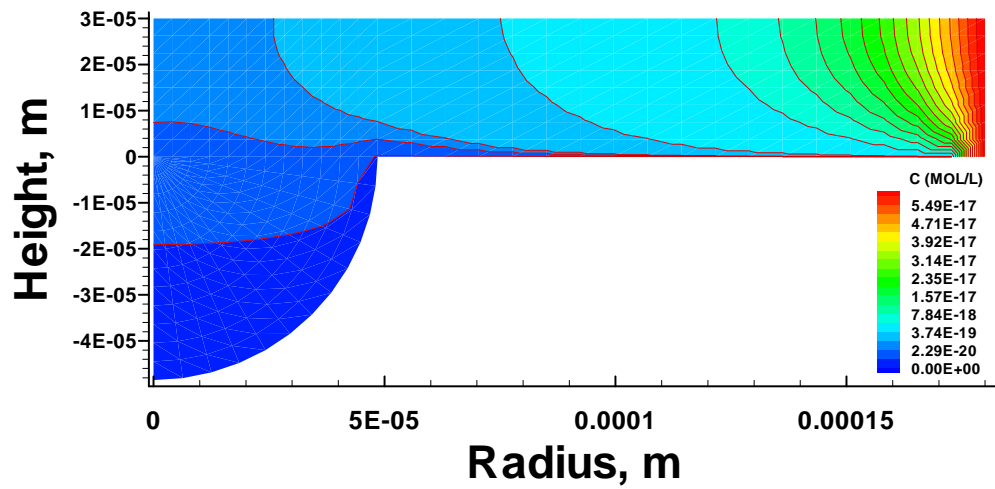


Figure 8 - Distribution of S^{2-} ion in the solution

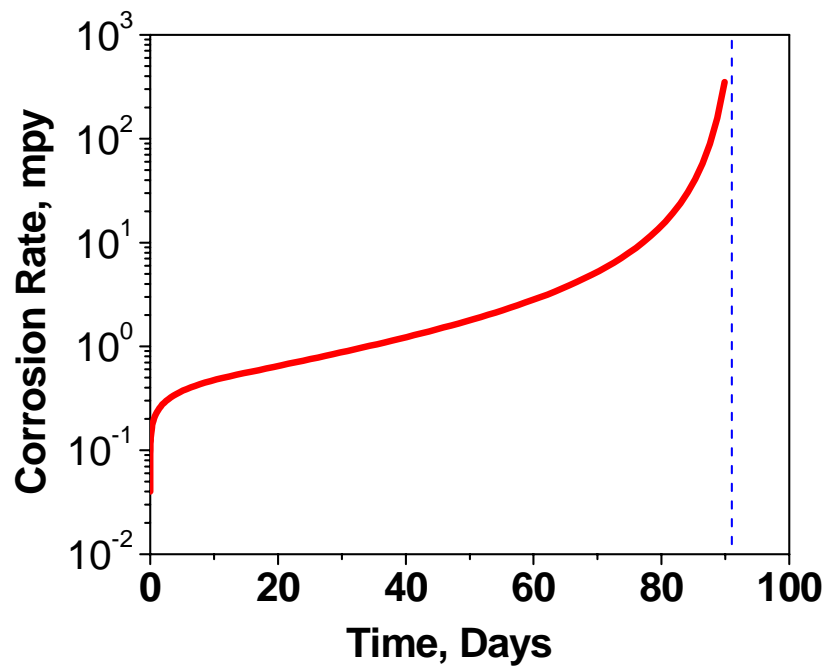


Figure 9 - Variation of pitting corrosion rate

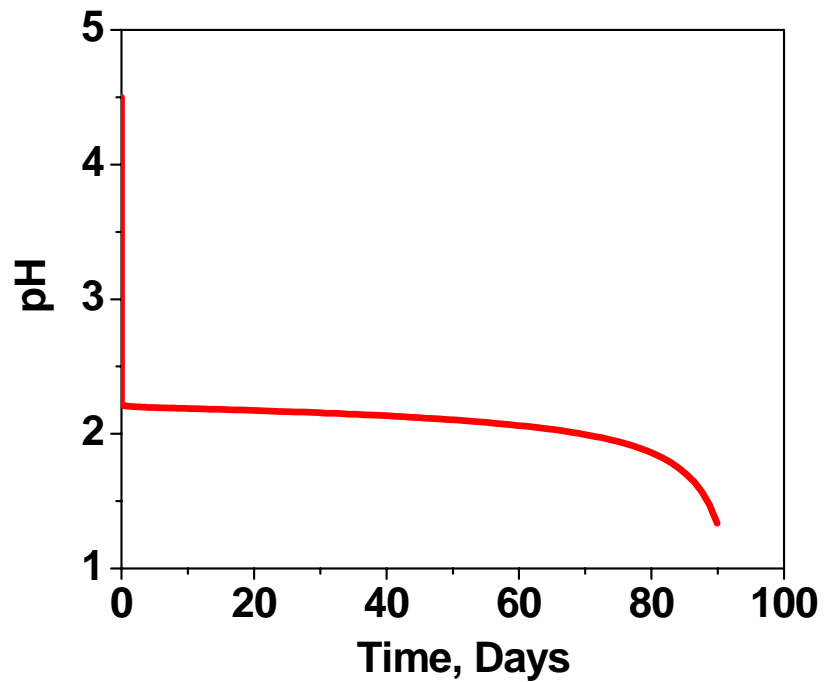


Figure 10 - Variation of pH value at anode

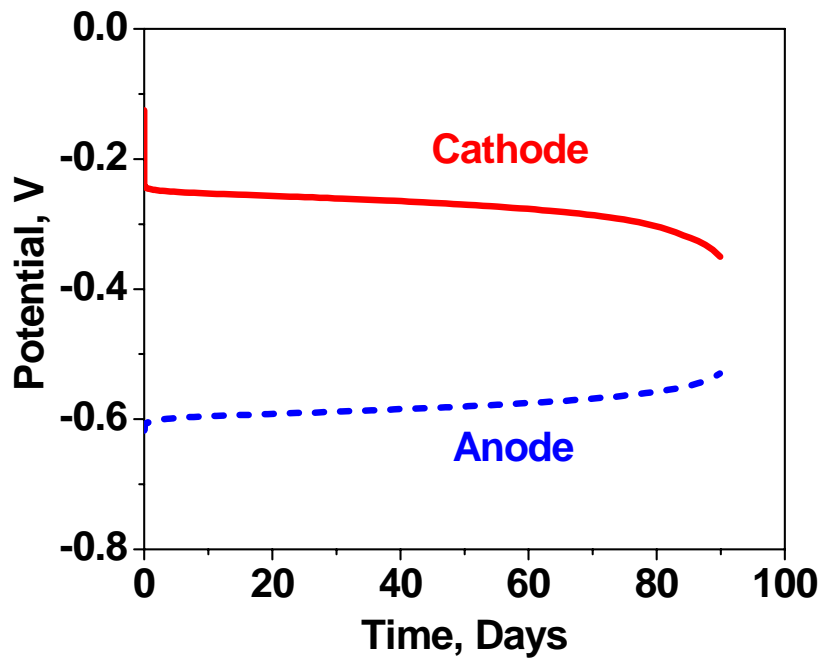


Figure 11 - Variations of anodic and cathodic potentials

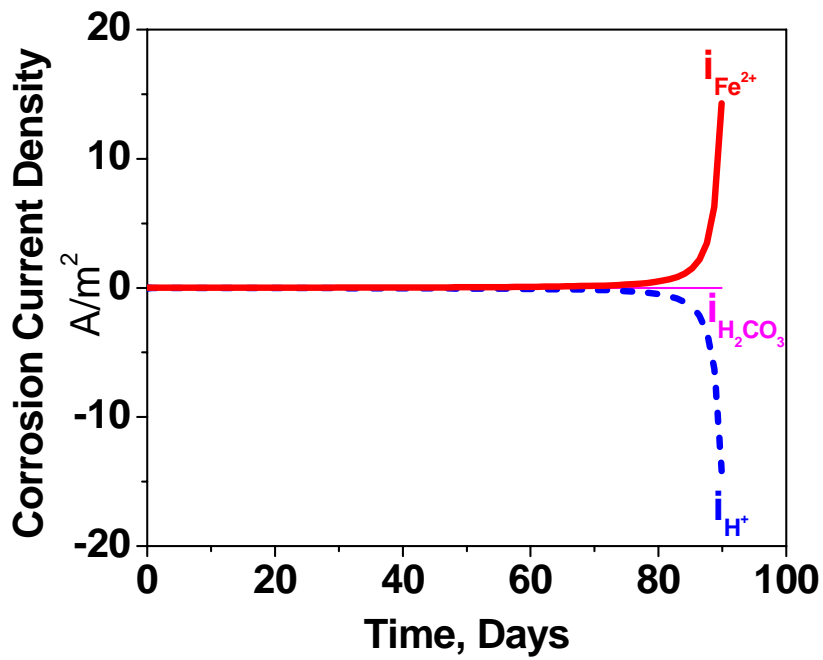


Figure 12 - Variations of corrosion current densities

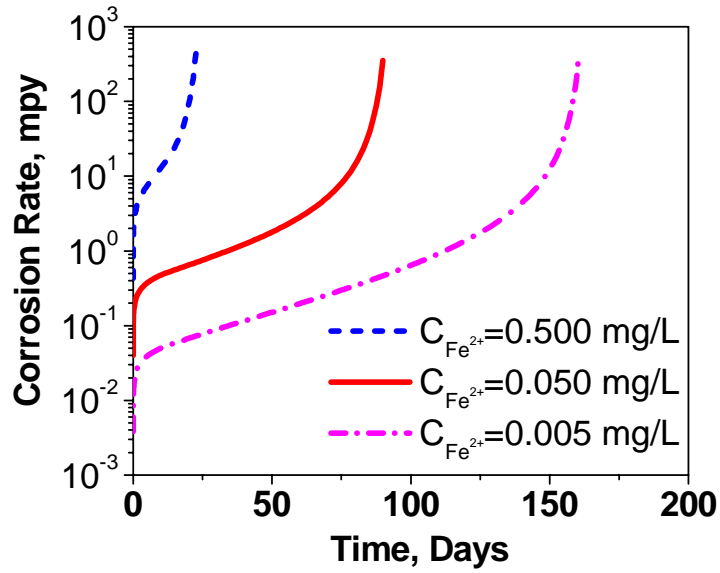


Figure 13 - Pitting corrosion rates with respect to initial iron ion concentration

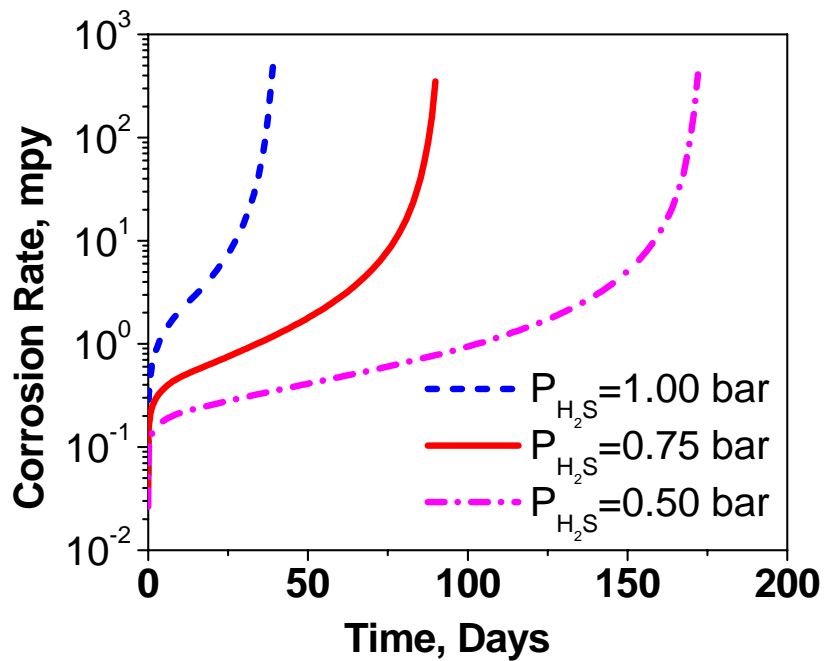


Figure 14 - Pitting corrosion rates as a function of partial pressure of H₂S

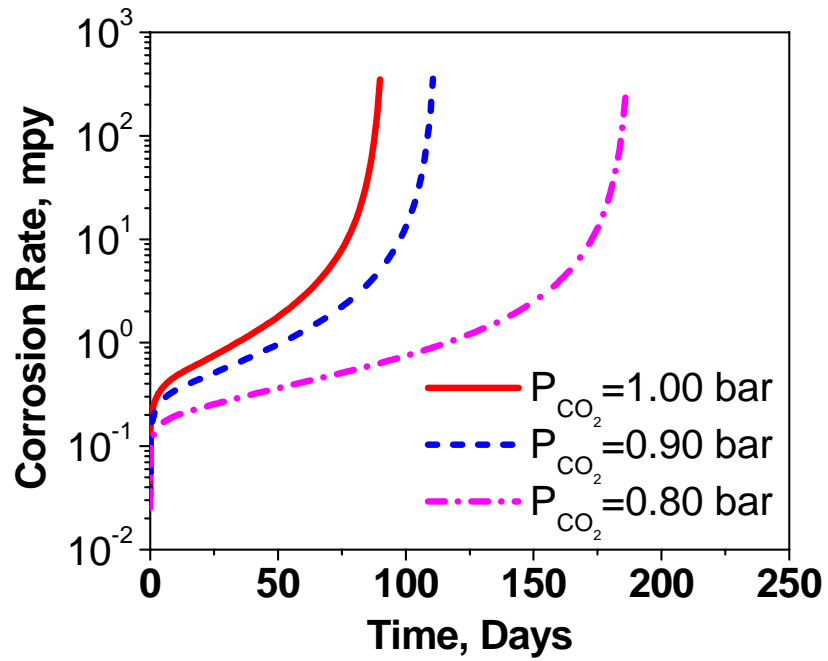


Figure 15 - Pitting corrosion rates as a function of partial pressure of CO₂

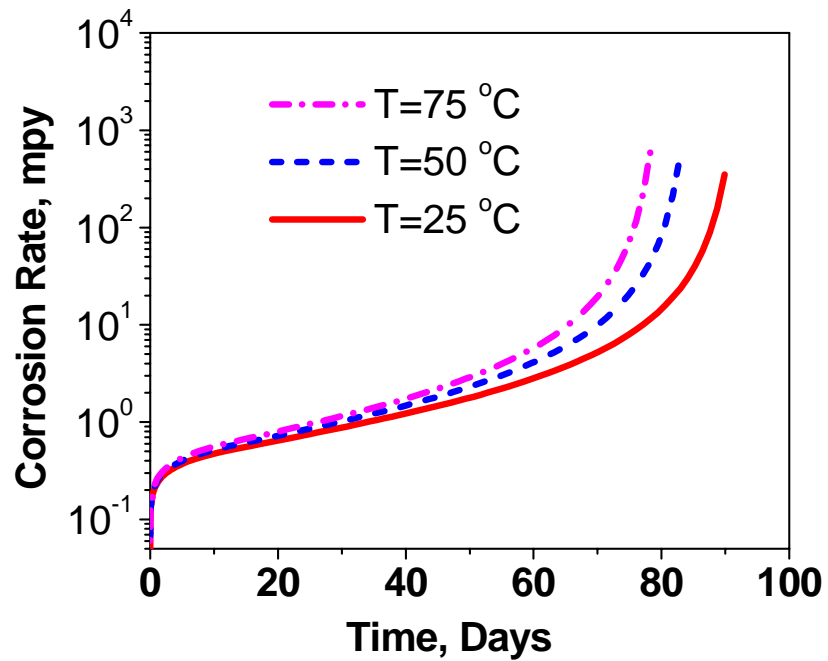


Figure 16 - Pitting corrosion rates as a function of environmental temperature